Impact of droplet oxidation on mechanical properties of an Al-7Si-0.4Mg alloy fabricated with liquid metal jetting

Sumit Bahl[1*], Gerry L. Knapp[1], Alexander Gomez[2], Jonathan D. Poplawsky[3], James A. Haynes[1], Ryan R. Dehoff[2], Alex Plotkowski[1], Amit Shyam[1]

[1]Materials Science and Technology Division
[2]Manufacturing Science Division
[3]Center for Nanophase Materials Sciences
Oak Ridge National Laboratory, Oak Ridge, TN 37830, USA

*Corresponding author, Email: bahls@ornl.gov

Abstract

Droplet-on-demand liquid metal jetting (DOD-LMJ) is a new method for additive manufacturing of bulk structural alloys. Here, we report on the microstructure, tensile, and fatigue properties of an Al-7Si-0.4Mg (A356) alloy fabricated with LMJ. Liquid metal droplets were shielded by high-purity Ar gas shroud during deposition. Atom probe tomography revealed that a few nanometers thick (Al-Mg-Si)-O oxide film formed on the droplets despite Ar gas shielding. Tensile tests on peak-aged LMJ A356 alloy showed that yield strength was isotropic (250 MPa), but ductility was lower in the build direction (6.1 ± 1.4%) compared to the transverse direction (9.4 ± 1.0%). Lower ductility in the build direction was attributed to delamination of metal-oxide interfaces at layer boundaries. The ductility and yield strength of LMJ A356 were similar to cast A356 and laser powder bed fused (LPBF) A357 alloys, indicating the limited impact of oxide film on tensile properties. The oxide film severely impacted the fatigue properties. Fatigue resistance of LMJ A356 was limited by fatigue crack initiation at lack-of-fusion defects and fatigue crack propagation along layer boundaries by delamination of the metal-oxide interface. The fatigue strength of LMJ A356 at 60 MPa was lower than cast A356 and LPBF A357 alloys in the peak-aged condition. This research underscores the need for managing droplet oxidation during LMJ additive manufacturing of structural alloys.

Keywords: Liquid metal jetting; Aluminum alloys; Oxidation; Tensile properties; Fatigue properties

1. Introduction

Droplet-on-demand liquid metal jetting (DOD-LMJ) is an additive manufacturing (AM) technology in which liquid metal droplets are deposited layer-by-layer to build 3-dimensional (3D) structures. The alloy feedstock is melted in a crucible and a variety of methods are used to jet a stream of liquid metal droplets from the orifice-end of the crucible onto a substrate. Various techniques of droplet generation are summarized in a review by Ansell [1]. Briefly, the droplets are jetted by applying either a mechanical force *via* a piezoelectric or pneumatic actuator or by using electric and/or magnetic fields to generate Lorentz force in liquid metal.

Liquid metal jetting offers new opportunities for metal AM that are distinct from existing technologies as described below:

Feedstock form agnostic: In-principle, LMJ is agnostic of the feedstock form because the feedstock (wire, powder, etc.) is melted and held in a reservoir before deposition. Owing to this capability, LMJ can simplify AM supply-chains and reduce cost by cutting the need to produce high-quality, expensive powder or wire feedstocks for powder-bed fusion (PBF) and directed energy deposition (DED) based AM methods.

Fill technological gap between PBF and DED AM: Powder bed fusion methods have the best-in-class feature resolution i.e., they can fabricate features as fine as a few hundred microns thick, but slow fabrication rates and high cost of powders are the limitations [2]. On the other hand, DED methods are much faster but cannot fabricate fine structures less than a few millimeters thick. The orifice size in LMJ controls the droplet size which, in turn, controls the minimum feature size. A wide range of droplet sizes in the order of ~ 50 – 1000 μm have been reported [3-7], which spans the range of PBF on one end and DED on the other end. Simultaneously, high frequency droplet deposition (order of 10^2 Hz) offers rapid fabrication with deposition rates in the order of 200 cc/h achievable [8]. This deposition rate is in between that of PBF (5-20 cc/h) and DED (up to 2000 cc/h) [2]. Liquid metal jetting offers the agility to tune the feature resolution and fabrication rates and could fill a technological gap between higher-resolution, lower build rate PBF processes and lower-resolution, higher build rate DED processes [9].

To name a few applications, LMJ can be suitable for cases where (1) a combination of deposition rate and feature resolution is required that cannot be fulfilled by PBF or DED, (2) it is difficult to produce high quality wire or powder feedstock, (3) powder handling is an issue, or (4) service repairs are required.

Aluminum alloys are among the commonly investigated materials in LMJ research because of their technological importance, and because their lower melting point poses fewer challenges for the printer hardware compared to other higher melting point materials like steels [10-13]. In an earlier study [10], Orme and Smith used Al droplets of 189 μm diameter generated using piezoelectric actuation to print Al cylinders up to 15 cm high. The printing was performed in an inert atmosphere as it was determined that oxygen contamination interfered with droplet jetting [11]. The printed parts exhibited minimal porosity, and it was shown that LMJ increased the ultimate tensile strength of the alloy by 30% compared to the ingot feedstock. Cao and Miyamoto [14] used pneumatic actuation to generate 200-800 μm diameter Al droplets and fabricated a few centimeters large Al structures in an inert atmosphere. They demonstrated that density of the printed part increased with velocity and size of the droplets and a maximum relative density of 92% was achieved. More recently, Gerdes et al. [13] demonstrated StarJet technology wherein liquid metal was forced through a star-shaped nozzle with a pneumatic actuator to fabricate 3D structures of an Al-12Si (wt%) alloy. The star-shaped nozzle reduced wall friction of droplets which prevented undesirable droplet deflection upon jetting [15]. Instead of using an inert chamber, an Ar gas shroud was used to prevent droplet oxidation.

The above-mentioned studies [11, 14, 15] exemplify that most lab-scale research has focused on the development of LMJ printing technologies while limited attention has been paid to microstructure-property relationships in LMJ printed alloys. One of the matured LMJ technologies has been recently commercialized with the trade name of ElemX [16]. The printer currently uses a 4008 Al wire feedstock which is chemically equivalent to the widely used structural cast A356 (Al-7Si-0.4Mg in wt%) alloy. The 4008 Al wire is continuously fed to a heated crucible where the wire melts and creates a reservoir of liquid metal. A pulsed magnetic field is applied to generate Lorentz force that pushes liquid metal droplets through a nozzle. The metal droplets are shielded by a high-purity Ar gas shroud.

The understanding of microstructure-property relationships in LMJ alloys is now beginning to emerge [17, 18]. The aim of this work is to study the microstructure-property relationships in an A356 Al alloy fabricated with LMJ, hereafter denoted as LMJ A356. Considering that liquid metal droplets were only locally shielded by Ar gas, the possibility of droplet oxidation was investigated. Atom probe tomography (APT) confirmed droplet oxidation occurred despite Ar protection. The surprising impact of droplet oxidation on the mechanical behavior of LMJ alloys is reported. Insights into the effect of droplet oxidation on tensile and fatigue properties of LMJ A356 will enable process improvement and alloy design for LMJ.

2. Methods

2.1. LMJ fabrication and heat-treatment

Cubes of 50 x 50 x 50 mm^3 or 20 x 20 x 20 mm^3 dimensions and cylinders of 105 mm length and 15 mm diameter with cylindrical axis parallel to the build direction were fabricated with an ElemX printer using the standard, manufacturer recommended processing parameters for A356 (4008 Al wire feedstock). The schematic of the LMJ process is shown in Fig. 1a. The printhead consisted of a resistively heated reservoir to store liquid metal and the reservoir was fed by the wire feedstock from the top. The upper portion of the reservoir was made with boron-nitride, and it was attached to a graphite nozzle at the bottom with a bore diameter of 470 µm. The reservoir was surrounded by a coil winding excited by a pulsed voltage. Each voltage excitation produced a magneto-hydrodynamic force in the liquid metal resulting in ejection of a single droplet [19]. The droplets were deposited on a heated build plate positioned underneath the printhead. The build plate moved horizontally (X and Y directions) with the print-head remaining stationary during deposition of one layer. The print-head moved vertically upwards (Z direction) to deposit the next layer. The liquid metal was held at 825 °C in the reservoir and droplets were deposited at a maximum of 400 Hz frequency on the build plate with an 8 mm working distance between the orifice and the build plate. The build plate was heated to 475 °C from the underside as recommended by the manufacturer and the temperature at the plate surface was manually measured to be ~ 440 °C. Such a high build temperature ensures high density in the printed samples as demonstrated by Traxel et al. [18]. The scanning direction for droplet deposition was rotated by 45° each layer. The printing parameters are summarized in Table 1. The fabricated parts were removed from the build plate by water-quenching the part attached to the build plate. Differences in thermal expansion behavior between the Ni-coated build plate and the deposited A356 alloy facilitated part removal without machining. The samples investigated in this study were printed in batches with build time per batch varying between 2 – 4 hours. Bulk oxygen content in 4008 Al wire feedstock and as-fabricated samples was measured by the inert gas fusion method. Some LMJ A356 samples were analyzed in the as-fabricated (AF) condition, denoted as LMJ A356-AF. Other samples were given a T6 heat-treatment, in which they were solutionized at 530 °C for 5 h and water quenched, followed by artificial aging at 160 °C for 5 h. This T6 treatment is the same as that used for cast A356 [20]. The T6 samples are hereafter denoted as LMJ A356-T6.

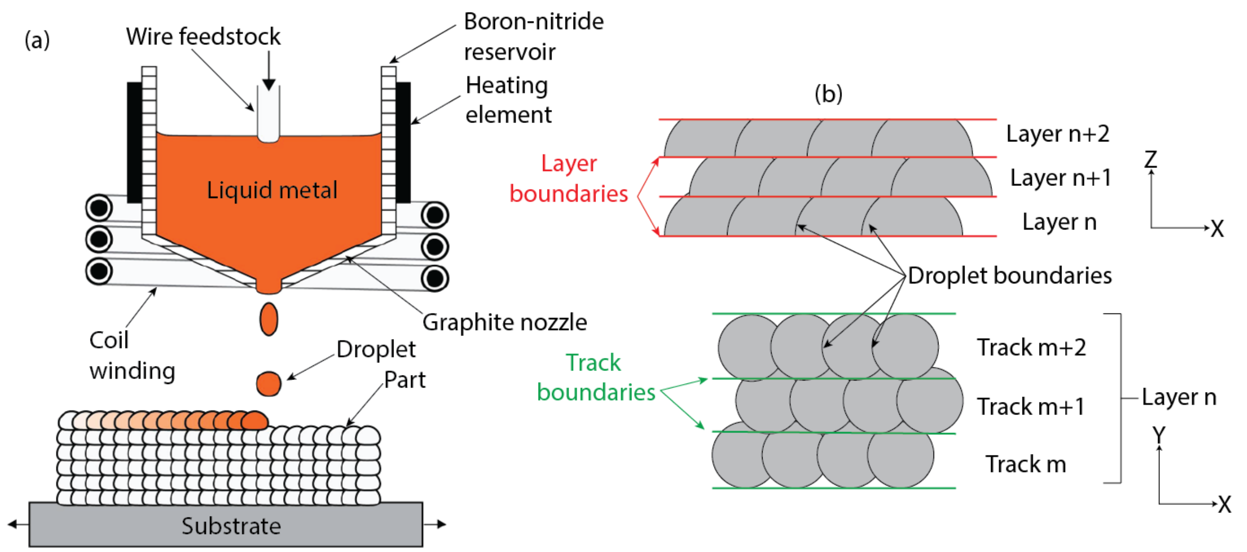

Figure 1 Schematic representations of (a) LMJ process and (b) layer boundaries, track boundaries, and droplet boundaries in an LMJ microstructure.

Table 1 List of printing parameters used in this study

Parameter	Value
Liquid metal temperature	825 °C
Bore diameter	470 µm
Jetting frequency	400 Hz
Substrate temperature	475 °C
Scan rotation angle	45°
Alloy	4008Al/A356

2.2. Microstructural characterization

The microstructures were characterized using a Tescan Mira 3 scanning electron microscope (SEM) equipped with EDAX electron backscatter diffraction (EBSD) and energy dispersive spectroscopy (EDS) detectors. Standard metallographic techniques were used to polish the samples with the final polishing performed using 0.05 µm colloidal silica solution. EBSD measurements were performed at 20 kV accelerating voltage, 25 mm working distance, and 1 µm step size. The results were analyzed using the TSL OIM software. The raw data was cleaned using Grain CI standardization method and only datapoints with confidence index greater than 0.1 were used in the analysis. A Zeiss Metrotom x-ray computer tomography (XCT) system was used to characterize the porosity in the samples. An accelerating voltage of 210 kV and beam current of 159 µA was used with a voxel size of 26.2 μm^3. The scanned volume was 28.98 mm x 31.86 mm x 31.13 mm, corresponding to 1106 x 1216 x 1188 voxels, and the data took approximately 23 minutes to collect. A minimum defect size of two voxels was used for defect analysis *via* the VGSTUDIO software. Archimedes method was used to measure absolute densities of as-fabricated samples and 4008 Al wire feedstock. The density was calculated by measuring sample weights in air and ethanol. Atom probe tomography was used to characterize the nanoscale microstructure using Cameca Instruments' LEAP4000 XHR. A Thermo Fisher Nova 200 dual beam focused ion beam-SEM was used to prepare APT needles following the standard lift-out procedure [21] as described in detail in our previous investigation [22]. The APT experiments were conducted at 70 K specimen temperature, 30% pulse fraction, 200 kHz pulse rate, and 0.3% detection rate. CAMECA's IVAS software (version 3.8) was used for APT data reconstruction and analysis.

2.3. Mechanical testing

Cylindrical tensile samples with 3 mm gauge diameter and 19 mm gauge length were machined with the loading axis parallel and perpendicular to the build direction in the as-fabricated and T6 conditions. Tensile tests were performed at room-temperature with an initial strain rate of ~ 10^{-4} s^{-1}. Tensile strain was measured using a 10 mm gauge length axial extensometer. High cycle fatigue (HCF) samples with 6.35 mm gauge diameter and 19.05 mm gauge length were machined from T6 aged cylindrical coupons with the loading axis parallel to the build direction. Room-temperature, load-controlled HCF tests were performed at 30 Hz frequency (sinusoidal waveform) and a stress ratio (R) of -1 until fracture or sample runout without fracture at 10^7 cycles. Fracture surfaces and cross-sections of tensile and fatigue samples were analyzed with SEM.

3. Results

3.1. Microstructure

Figure 2 shows the inverse pole figure (IPF) and image quality (IQ) EBSD maps of the planes parallel (XZ) and perpendicular (XY) to the build direction (Z) for LMJ A356-AF. The IPF maps of the XZ (Fig. 2a) and XY (Fig. 2c) planes show a fine equiaxed grain structure with an average grain diameter of ~ 9 ± 8 µm. Boundaries between overlapping layers are occasionally visible (albeit faintly) in gray-scale IQ map of the XZ plane, as indicated by the dashed line in Fig. 2b. However, boundaries between parallel deposition tracks in the same layer and inter-droplet boundaries in the same track are not discernible (see Fig. 1b for schematic of the different types of boundaries). The dashed line in Fig. 2d outlines the cross-section of an individual droplet. This droplet is rotated by 45° with respect to another partially noticeable droplet which is consistent with the 45° scan rotation between successive layers. The grain size is not uniform with finer grains closer to droplet boundaries and coarser grains in the remaining regions of the droplets (Fig. 2d). Epitaxial grain growth across layer boundaries occurred rarely with one such instance marked in Fig. 2a.

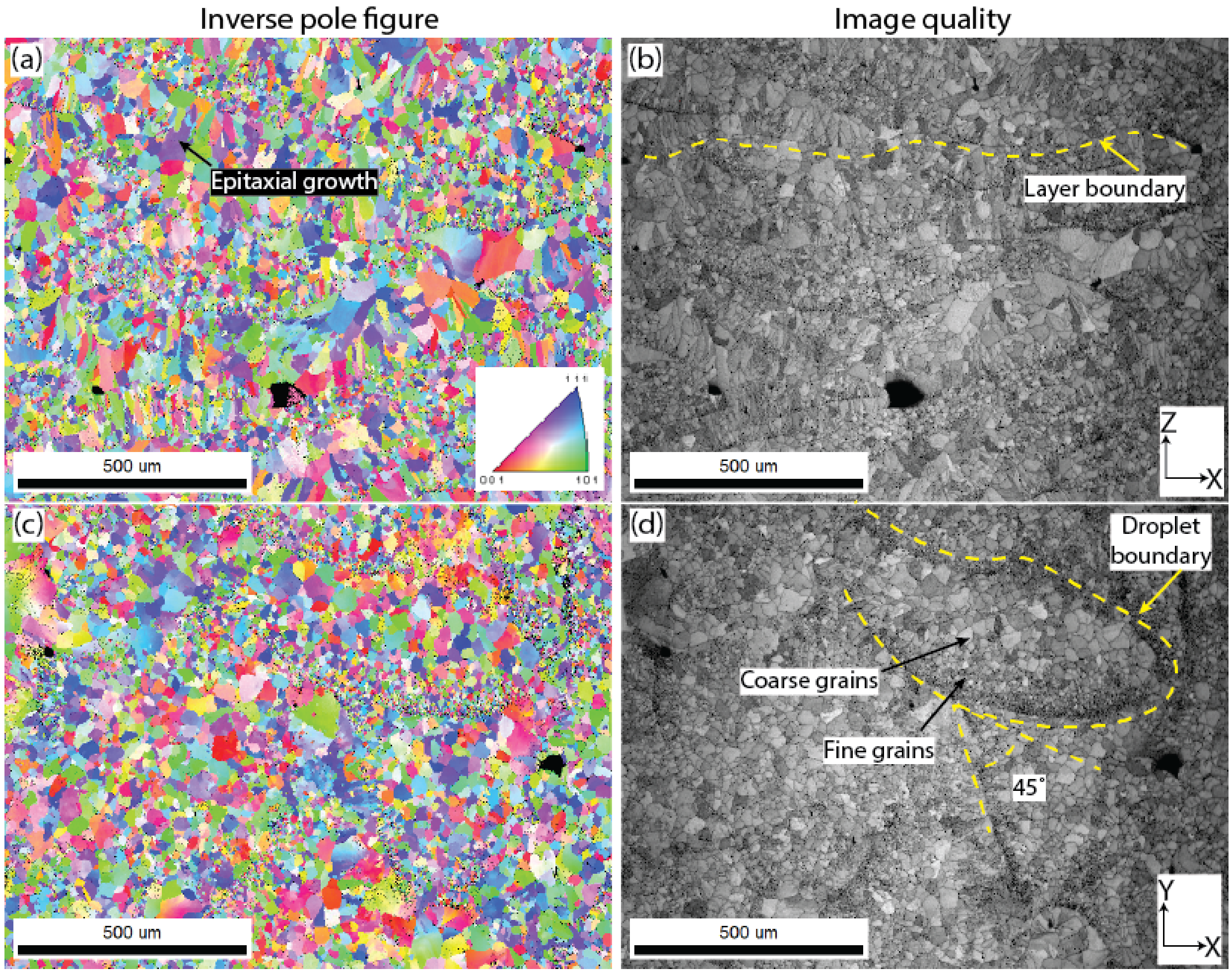

Figure 2 EBSD results of an LMJ A356-AF sample. IPF maps of (a) XZ and (c) XY planes and the corresponding IQ maps in (b) and (d), respectively. The build direction is along the Z-axis. The curved yellow dashed lines in (b) and (d) outline a layer boundary and the cross-section of an individual droplet, respectively.

Figure 3 shows secondary-electron (SE)-SEM images of LMJ A356-AF and LMJ A356-T6 samples. The as-fabricated microstructure (Fig. 3a) contains a uniform distribution of sub-micron sized Si particles whose identity is confirmed by EDS maps shown in supplementary Fig. S1. The Si particles, with an equivalent diameter of 0.48 ± 0.20 μm, have spheroidized due to in situ annealing during printing at a nominal build temperature of 475 °C with a total build time between 2 – 4 hours (Section 2.1). The exact Si particle size may vary from sample to sample due to differences in the total build time and the corresponding extent of the in situ annealing effect; however, the effect of build time on Si particle size is not investigated in this study. As shown in

Fig. 3b, Si particles have coarsened to 1.36 ± 0.54 µm equivalent diameter after the T6 treatment. The T6 treatment also results in the formation and/or growth of pre-existing plate-shaped Al-Fe-Si intermetallics as marked by the arrows in Fig. 3b. The EDS map shown in supplementary Fig. S2 confirmed that these are Al-Fe-Si intermetallic particles and could potentially be the β-Al_5FeSi phase based on the plate-shape morphology. The grain diameter increased negligibly from 9 ± 8 µm in the as-fabricated condition to 14 ± 11 µm after T6 treatment (supplementary Fig. S2). Overall, the AF and T6 microstructures are consistent with those reported by the ElemX manufacturer [23].

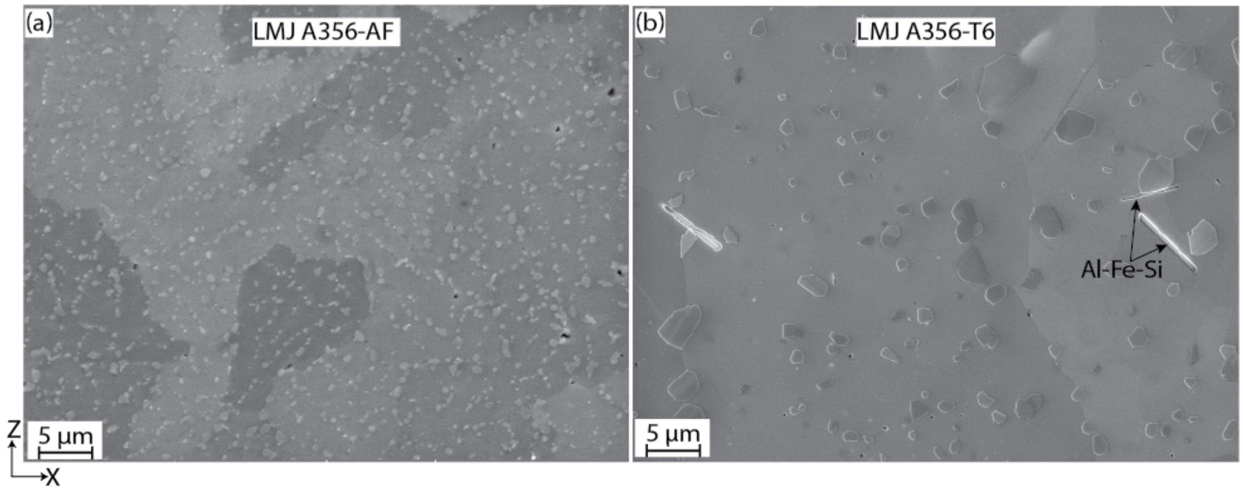

Figure 3 SE-SEM images on XZ plane of (a) LMJ A356-AF and (b) LMJ A356-T6 alloys. Both microstructures are characterized by spheroidized Si particles with a larger particle size in LMJ A356-T6. The arrows in (b) mark the plate-shaped Al-Fe-Si intermetallics.

Typical processing defects identified in LMJ A356 alloy are shown in Fig. 4. The defects are located at layer boundaries and inside individual droplets. The defects at layer boundaries are lack-of-fusion defects which occur in various morphologies with some of the frequently observed morphologies shown in Fig. 4a-c. Each morphology type indicates a different cause for the defect formation. The defect in Fig. 4a has a triangular morphology and appears to form due to incomplete fusion at the base of two overlapping droplets in a layer. The other type of defect in Fig. 4b is spherical which is likely related to gas entrapment. Figure 4c shows another type of triangular defect with an inverted morphology formed at the cusp of two overlapping droplets in one layer incompletely filled by the droplet in the layer above. Another kind of defect located inside individual droplets is shrinkage porosity similar to those found in cast alloys, as shown in Fig. 4d.

The size distribution and volume fraction of defects were quantified with XCT. Figure 5a shows the spatial distribution of defects in an LMJ A356-AF sample and the corresponding size distribution is plotted in Fig. 5b. As seen in Fig. 5a, the largest defects are generally restricted to the first few layers while majority of the sample volume contains comparatively smaller defects. It is unknown if the largest defects are always restricted to the first few layers in every build or this behavior was limited to the particular sample scanned for XCT. The defect size (equivalent diameter) follows a log-normal distribution with a peak value of ~ 130 µm. Overall, the LMJ

A356-AF sample is highly dense with only 0.1 vol% of total porosity. A porosity of 0.13% was determined by analyzing a large area (~ 7×7 mm^2) of an LMJ A356-AF sample under SEM. Archimedes method determined the absolute densities of LMJ A356-AF sample and 4008 Al wire (considered to be fully dense i.e. zero porosity) to be similar at 2.65 and 2.63 g/cm^3, respectively. The similar densities of LMJ A356-AF sample and 4008 Al wire suggest a very low porosity in the printed condition in agreement with the XCT and SEM analysis.

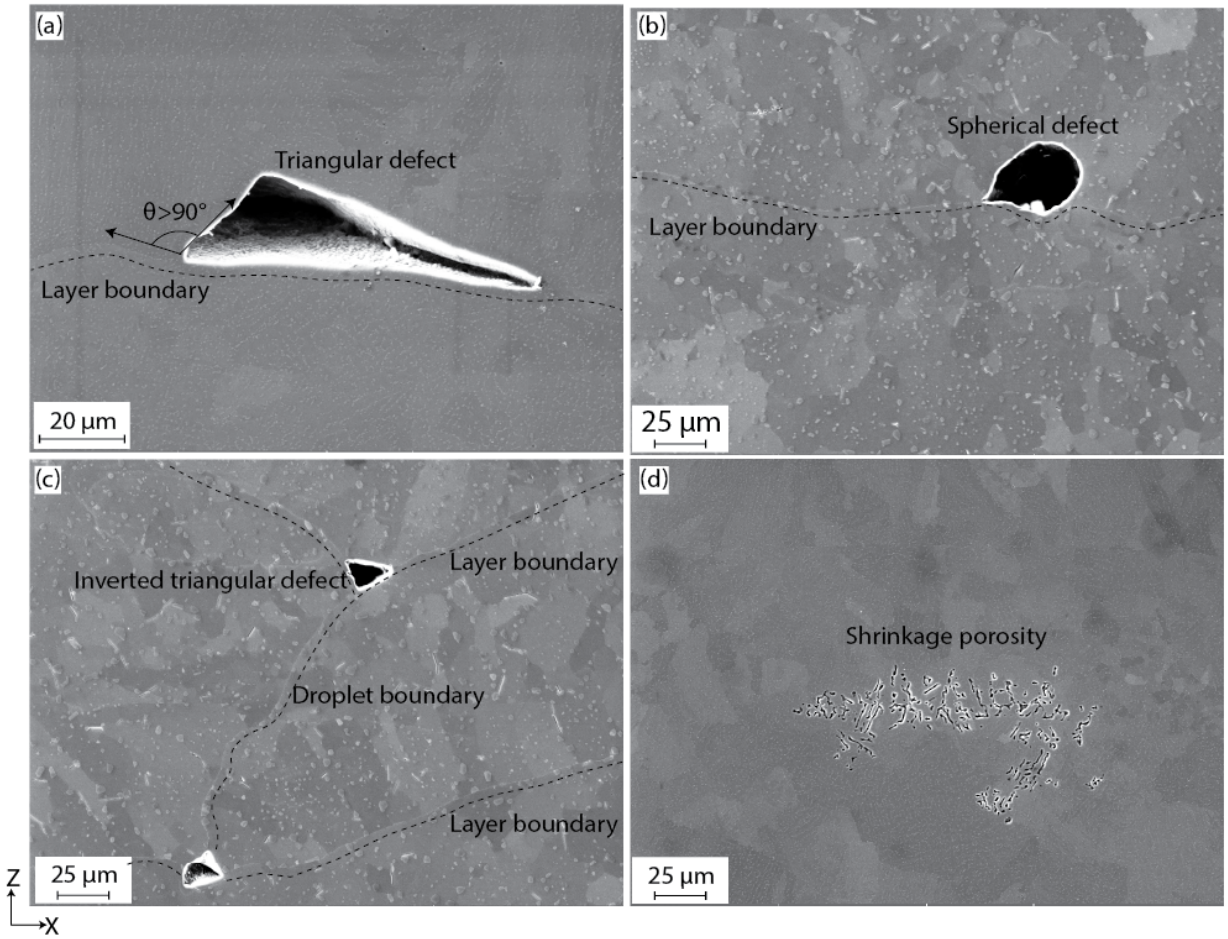

Figure 4 SE-SEM images of the XZ plane showing the commonly observed defect types in LMJ A356. The images in (a-c) show lack-of-fusion defects with diffferent morphologies in (a) LMJ A356-AF and (b, c) LMJ A356-T6 samples. The as-fabricated and T6 samples have similar types of defects. The dotted lines in (a, b) mark the layer boundaries and in (c) mark the layer boundaries as well as the droplet boundary between overlapping droplets in the same layer. The solidification contact angle of the droplets with the lack-of-fusion defect in (a) is θ>90°. The image in (d) shows a small network of shrinkage porosity inside one of the droplet in LMJ A356-AF.

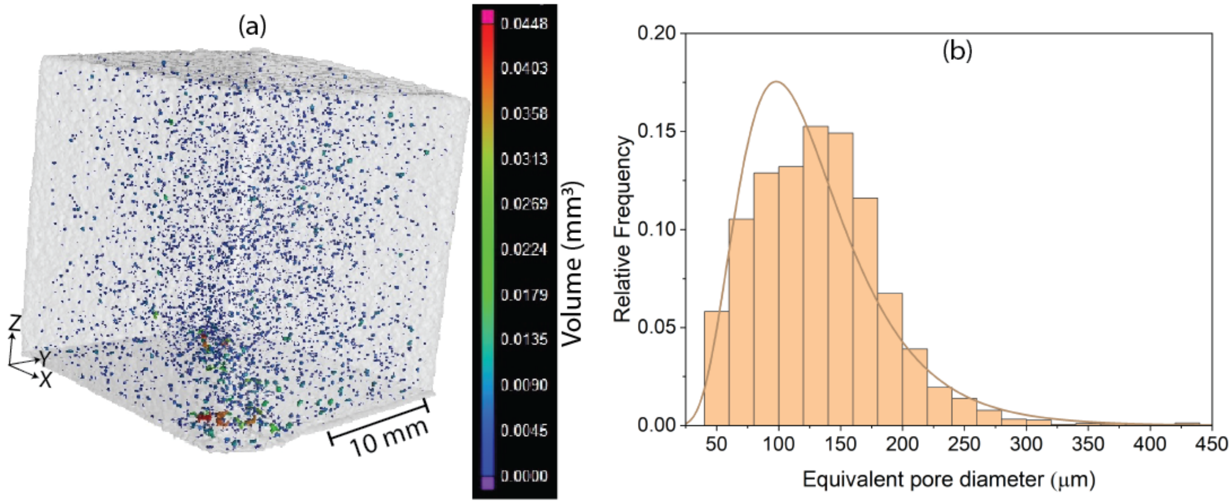

Figure 5 X-ray computed tomography results of LMJ A356-AF sample. (a) Spatial distribution of porous defects in a cube of approximately 20 mm^3 volume with the corresponding defect size distribution plotted and fitted to a log-normal distribution in (b).

3.2. Atom probe tomography

Nanoscale microstructure of LMJ A356-T6 was analyzed with APT. The reconstructed 3-dimensional (3D) atom maps in Fig. 6a show the distribution of individual atomic species in an APT needle containing a layer boundary. The results clearly reveal that the layer boundary is coated with a few nanometers thick and continuous oxide film. Inert gas fusion method determined that 4008 Al wire feedstock contains less than 50 ppm of oxygen and it increases to 58 ppm in the as-fabricated material. This result suggests that interaction with ambient environment oxidizes droplets during LMJ printing. The oxide is enriched in Al, Si, and Mg and their individual concentrations are plotted in the proximity histogram in Fig. 6b. APT was also performed in regions away from the layer boundary. The atom maps in Fig 6c show needle-shaped Mg-Si rich nanoscale precipitates formed due to the T6 aging. The oxygen atom map is not shown in Fig. 6c since no oxide layer was observed in region away from the layer boundary. The Mg:Si ratio in the precipitates is approximately equal to 1.1, as shown by the proximity histogram in Fig. 6d. Based on the needle morphology, nanoscale size, and Mg:Si ratio of ~1.1 these precipitates are expected to be β″ phase in the Al-Si-Mg system and are the key strengthening precipitate for the current alloy [24]. APT results indicate that the nanoscale precipitates also contain a significant amount of dissolved Al atoms which is consistent with previously reported compositions of β″ precipitates measured with APT [25-27]. The exact precipitate composition cannot be determined with APT due to small precipitate size and aberrations at the precipitate/matrix interface. Transmission electron microscopy is required to confirm the phase of the nanoscale precipitates. For the purpose of this study, the nanoscale precipitates are referred to as Mg-Si precipitates.

In contrast to copious Mg-Si precipitation away from layer boundaries (Fig. 6c), precipitation is not observed near the oxide film (Fig. 6a). Table 2 summarizes Al matrix compositions in the APT needles of Fig. 6a and c. Despite precipitation of solute atoms, the Al matrix concentrations of ~0.1 at% Mg and ~0.6 at% Si in the needle with Mg-Si precipitates are higher than ~0.05 at% Mg and ~ 0.29 at% Si matrix concentrations near the oxide film without the precipitates. Depleted Mg and Si solute concentrations and lack of Mg-Si precipitates in Al matrix adjacent to the oxide film correlates well with Mg and Si enrichment in the oxide film. Additional APT samples, numbered as '1-4' in Fig. 7a, were prepared in a region close to a layer boundary with needle '1' and '4' being the farthest and nearest to the layer boundary, respectively. The reconstructed atom maps with Mg isoconcentration surfaces outlining the Mg-Si precipitates are shown for the needles in Fig. 7b. The needles '1-3' farther from the layer boundary have uniformly dispersed Mg-Si precipitates similar to Fig. 6c. On the other hand, the APT needle closest to the layer boundary shows sparsely populated Mg-Si precipitates. The complete lack of Mg-Si precipitation in the immediate vicinity of the oxide film (Fig. 6a) and limited precipitation in the nearby regions (Fig. 7b, needle '4') is indicative of a precipitate free zone (PFZ) along the oxidized layer boundary.

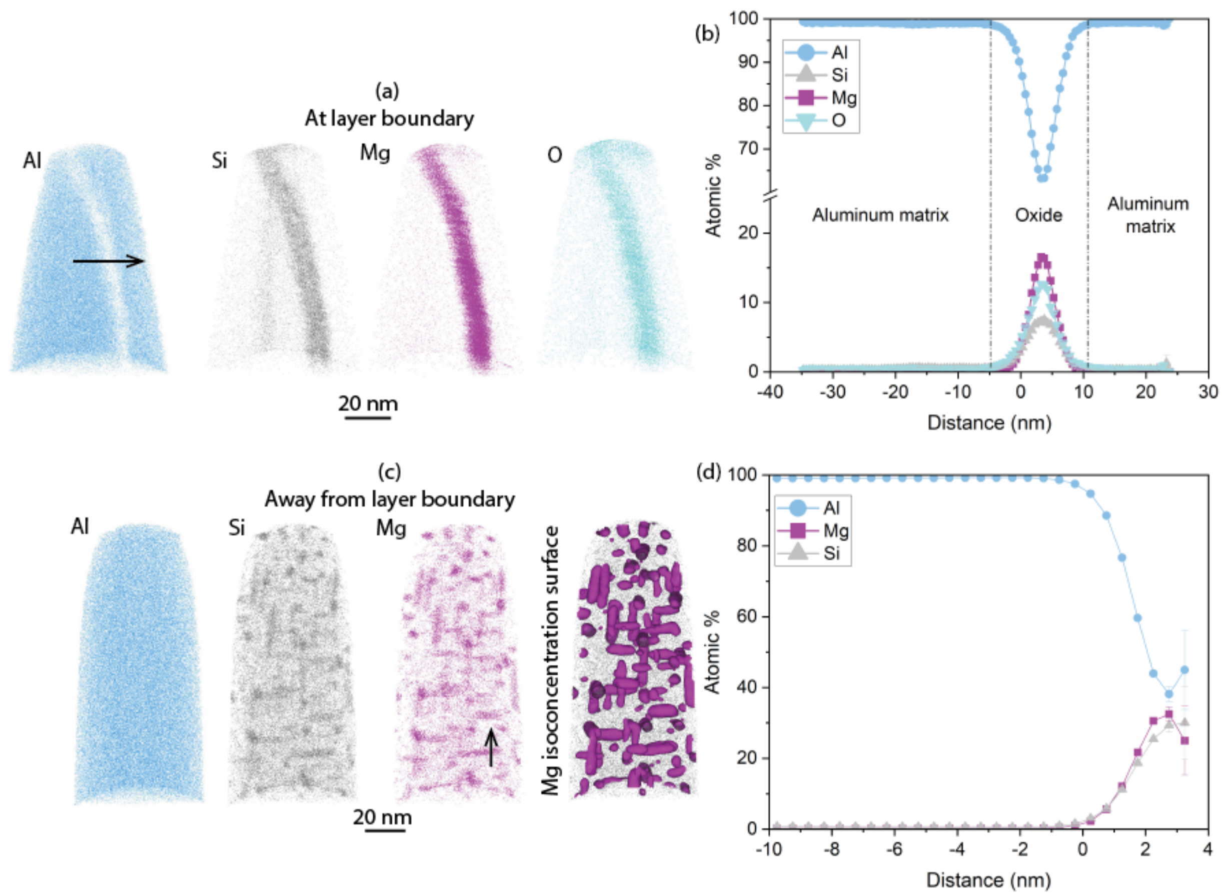

Figure 6 Atom probe tomography results of an LMJ A356-T6 sample. (a) Reconstructed 3D atom maps showing the distribution of individual atomic species at a layer boundary. The presence of a thin oxide film at the layer boundary is confirmed. (b) Proximity histogram across the metal-oxide-metal interface indicated by the arrow in the Al atomic map in (a). (c) Individual atom maps and a map with Mg isoconcentration surfaces drawn in purple for a region away from the layer boundary showing nanoscale Mg-Si precipitates. (d) Proximity histogram averaged over multiple matrix/precipitate interfaces with one such interface indicated by an arrow in the Mg atom map in (c). The precipitates have a Mg:Si ratio of ~ 1.1. The small precipitate size and aberrations at the precipitate/matrix interface make it impossible to determine the exact precipitate composition.

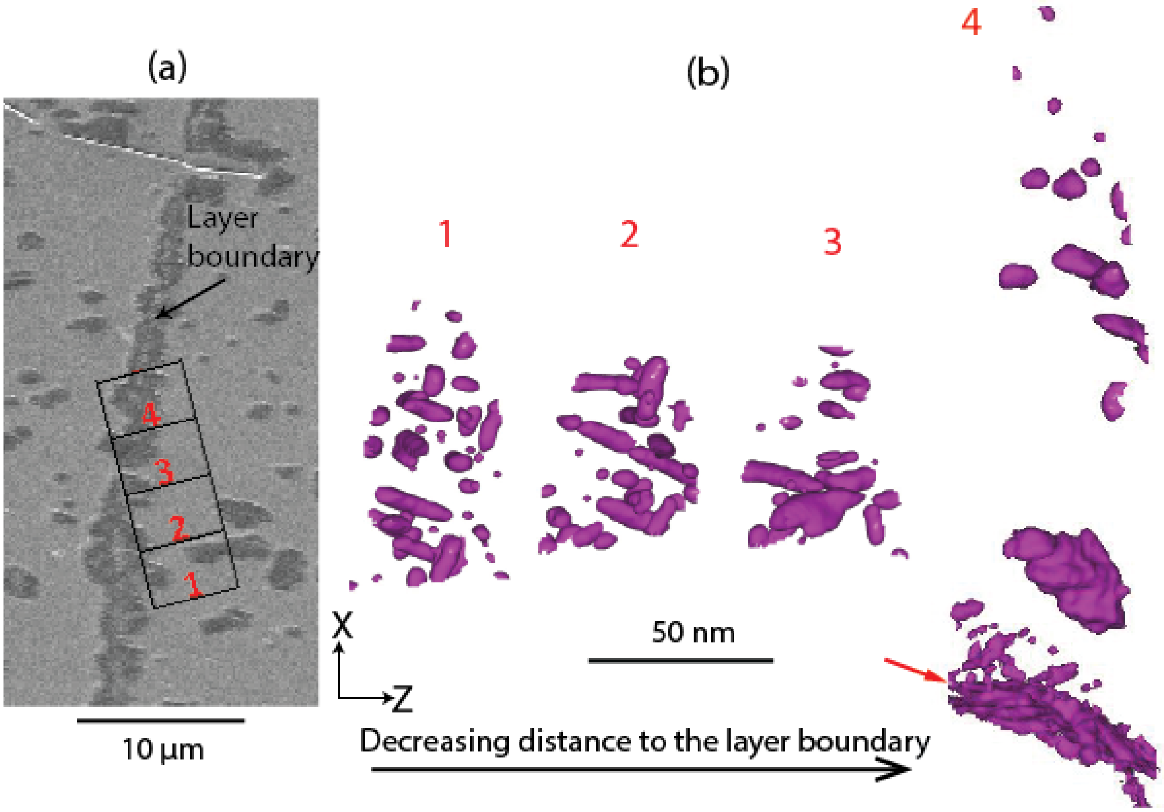

Figure 7 (a) SEM image of an LMJ A356-T6 sample containing a layer boundary. APT needles were analyzed from locations marked '1-4' with '1' being the farthest and '4' the nearest to the layer boundary. (b) 3D reconstructions with Mg isoconcentration surfaces illustrating the difference in Mg-Si precipitation behavior close to the layer boundary ('4') and away from the layer boundary ('1-3'). The red arrow at the bottom edge in needle '4' points to Mg segregation at a Si particle/matrix interface.

Table 2 APT measured composition of the Al matrix in at% near the oxide film without Mg-Si precipitates (Fig. 6a) and away from the oxide with copious Mg-Si precipitates (Fig.6c).

	Al	Mg	Si	O
Near oxide film (w/o Mg-Si precipitates)	99.38 ± 0.01	0.05 ± 0.01	0.29 ± 0.01	0.02 ± 0.01
Away from oxide film (w/ Mg-Si precipitates)	99.32 ± 0.01	0.10 ± 0.01	0.58 ± 0.01	-

3.3. Tensile properties

Room-temperature tensile properties of LMJ A356-AF and LMJ A356-T6 samples were measured parallel and perpendicular to the build direction, hereafter denoted as vertical and horizontal directions, respectively (also schematically shown in Fig. 8). The engineering stress-strain curves are shown in Fig. 8 and the properties are summarized in Table 3. The yield strength (YS) and ultimate tensile strength (UTS) are similar in the vertical and horizontal directions for a given condition (as-fabricated or T6). The YS and UTS increase from 110 MPa and 165 MPa in LMJ A356-AF to 250 MPa and 320 MPa, respectively, in LMJ A356-T6. The ductility exhibits a larger sample-to-sample variability in LMJ A356-AF and it is similar between the vertical (18.3 ± 3.1%) and horizontal (21.0 ± 5.6%) directions. Note that one of the three LMJ A356-AF vertical samples fractured prematurely (<5% ductility) due to a large defect, therefore, this sample was excluded from calculating the average ductility of 18.3 ± 3.1%. The T6 treatment reduced the ductility from 18.3 ± 3.1% to 6.1 ± 1.4% and from 21.0 ± 5.6 % to 9.4 ± 1.0% in the vertical and horizontal directions, respectively. The horizontal direction is more ductile compared to the vertical direction in the T6 condition. The plastic region of the stress-strain curves are serrated for LMJ A356-AF but not for LMJ A356-T6. The serrations in LMJ A356-AF resemble those due to Portevin–Le Chatelier (PLC) effect [28, 29] but further work is needed to identify the underlying cause of serrations.

Table 3 compares the tensile properties of LMJ A356 to (i) cast A356 and (ii) A357 alloy produced with laser powder bed fusion (LPBF) additive manufacturing. Alloy A357 is similar to A356 in composition but with a higher Mg concentration of 0.6 wt% compared to 0.4 wt% in A356. LPBF A357 was chosen for comparison because a self-consistent study reporting both tensile and fatigue properties of this alloy was available [30]. The properties of cast A356 are taken from two different studies [31, 32]. In T6 condition, LMJ A356 tensile properties are similar to that of cast A356 (denoted as cast A356-T6) and LPBF A357 (denoted as LPBF A357-T6). Comparing the as-fabricated state between the two AM techniques, LMJ A356-AF has a lower strength and higher ductility than as-fabricated LPBF A357 (denoted as LPBF A357-AF).

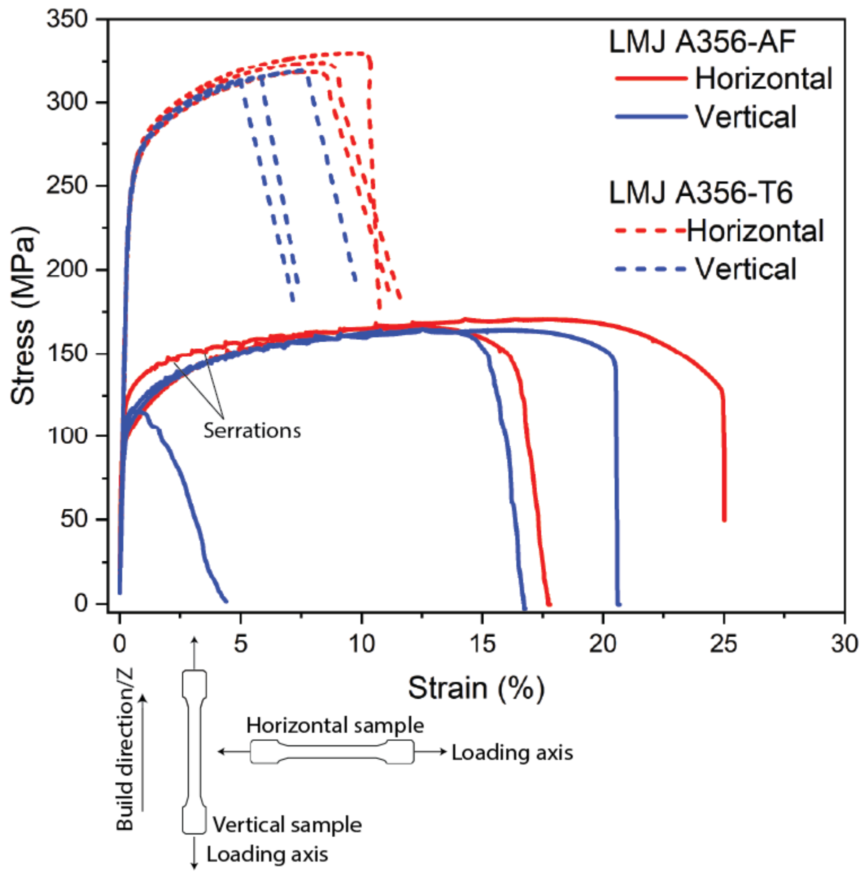

Figure 8 Room-temperature engineering stress-strain curves of LMJ A356-AF and LMJ A356-T6 samples in the horizontal and vertical directions. The schematic in the bottom shows orientation of vertical and horizontal tensile samples with respect to the build direction.

Table 3 Tensile properties of LMJ A356-AF and LMJ A356-T6 and their comparison with cast A356-T6, LPBF A357-AF, and LPBF A357-T6. The LPBF A357-AF samples were printed on a build platform at 35 °C [33]. The build platform temperature for LPBF A357-T6 samples was not reported [30]. The T6 treatment used for LMJ A356 and cast A356 alloy marked as (a) is the same [31]. The T6 treatment conditions were not reported for cast A356 alloy marked (b) but were noted to be the standard conditions [32]. The T6 treatment for LPBF A357 (543 °C/1.5 h solutionizing followed by 160 °C/8 h aging) is similar to that for LMJ A356 [30]. LPBF A357-T6 samples were stress-relieved at 300 °C for 2 h prior to solutionizing and properties in the vertical direction are reported.

Alloy		**YS (MPa)**		**UTS (MPa)**		**Elongation (%)**	
		Vertical	Horizontal	Vertical	Horizontal	Vertical	Horizontal
LMJ	AF	107 ± 4	110 ± 15	165 ± 1	168 ± 3	18.3 ± 3.1	21.0 ± 5.6
	T6	251 ± 2	253 ± 2	316 ± 3	324 ± 6	6.1 ± 1.4	9.4 ± 1.0
Cast A356 (a) [31]	T6	232		301		8.6	
Cast A356 (b)	T6	256-272		279-288		5.2-7.3	

[32]				
LPBF A357 [30, 33]	AF	195	350	4.5
	T6	271	327	7.3

Fractographs of the tensile samples are presented in Fig. 9. LMJ A356-AF vertical sample has a dimpled fracture surface typical of ductile fracture (Fig. 9a, b). The fracture surface of LMJ A356-AF horizontal sample is markedly different, where unlike the vertical sample, layer boundaries are clearly revealed suggesting their role in fracture (Fig. 9c). It appears that cracks are initiated by shear failure at layer boundaries. Subsequently, the sample fractured in a ductile manner as evidenced by the dimpled appearance of the fracture surface (Fig. 9d). Lack-of-fusion defects are visible on the fracture surfaces of both the vertical and horizontal samples as marked by arrows in Fig. 9a and c, respectively, pointing to their contribution in limiting the ductility. The fractograph of the LMJ A356-AF vertical sample with less than 5% elongation (that was excluded from calculating the average ductility, Fig. 8) is shown in supplementary Fig. S3. The fracture surface is complicated consisting of large defects resembling shrinkage porosity (Fig. S3b) and smooth regions devoid of ductile dimples (Fig. S3c). The nature of these defects and their origin is unclear and requires further investigation.

The fracture mode in the vertical sample changes after the T6 treatment (Fig. 9e, f). The parallel deposition tracks in a printed layer and the individual droplets in each track are visible on the fracture surface (Fig. 9e) indicating that fracture occurred by delamination at the layer boundary. This behavior is unlike the typical ductile fracture with limited-to-no role of layer boundaries in the as-fabricated vertical sample (Fig. 9a,b). The magnified view of the fracture surface (Fig. 9f) has a unique appearance consisting of Si particles and dendrite-like features without dimples. It is speculated that the dendrite-like features are related to the oxide film, but understanding this relationship is beyond the scope of this work. The fracture surface of the LMJ A356-T6 horizontal sample (Fig. 9g-h) is similar to its as-fabricated counterpart (Fig. 9c-d) indicating that the fracture initiated by shear failure at layer boundaries and subsequently grew by ductile (dimpled) fracture.

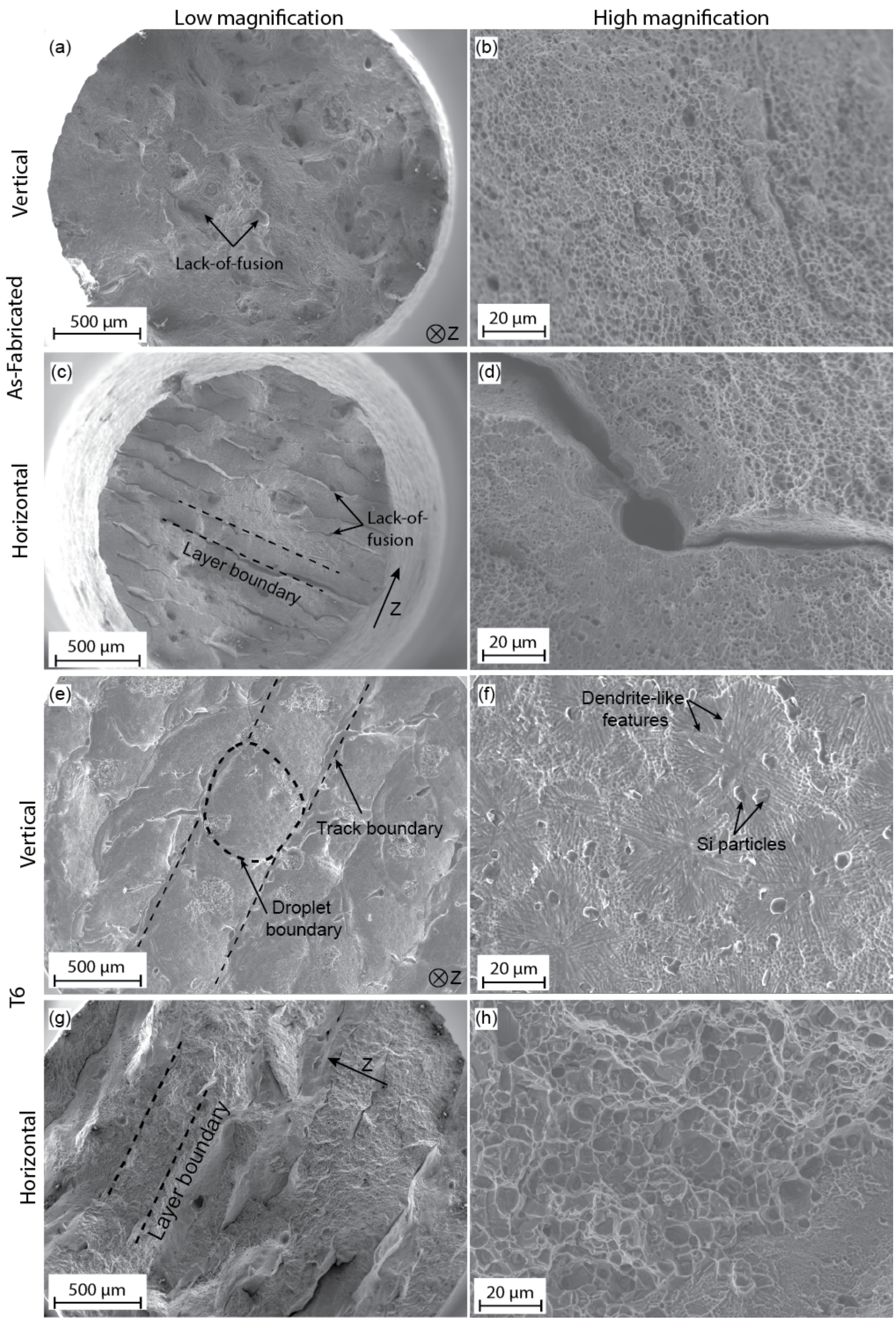

Figure 9 Fractographs of (a-b, e-f) vertical and (c-d, g-h) horizontal LMJ A356 tensile samples in (a-d) as-fabricated and (e-h) T6 conditions. The left and right columns show lower magnification and higher magnification images, respectively.

3.4. Fatigue properties

Room-temperature fully reversed (R = -1) HCF tests were performed on vertical LMJ A356-T6 samples. The vertical direction exhibits similar yield strength but lower ductility than the horizontal direction. The relatively lower mechanical properties in the vertical direction are expected to provide a conservative estimate of the fatigue strength. Figure 10 shows the results of the HCF tests and compares them to cast A356-T6 (a) and (b) and LPBF A357-T6 alloys (Table 3) reported in literature [30-32]. LMJ A356-T6 exhibits a consistently lower fatigue life over a broad range of stresses compared to cast A356-T6 (a) and (b) and LPBF A357-T6. The fatigue strength defined by specimen runout without fracture at 10^7 cycles is 60 MPa for LMJ A356-T6 compared to 90 MPa, 70 MPa, and 200 MPa for cast A356-T6 (a), cast A356-T6 (b), and LPBF A357-T6, respectively.

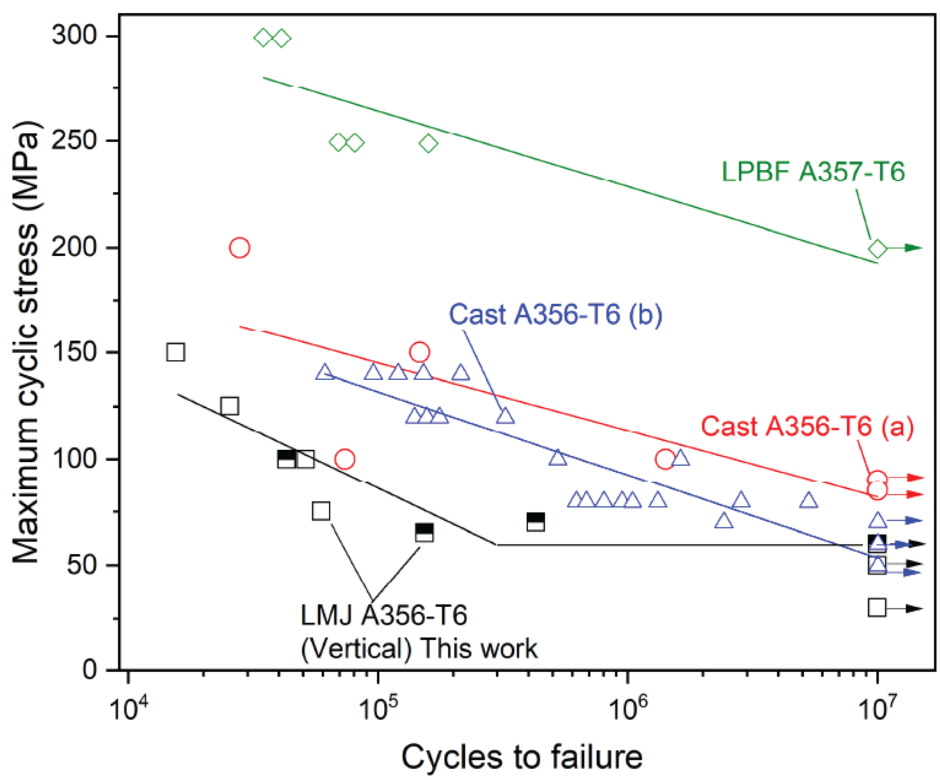

Figure 10 Room-temperature high cycle fatigue results of vertical LMJ A356-T6 samples compared to cast A356-T6 (a) [31], cast A356-T6 (b) [32], and LPBF A357-T6 [30] alloys. The arrows indicate specimen runout without fracture at the end of 10^7 fatigue cycles. The open and half-filled black square symbols are of vertical LMJ A356-T6 samples printed in two separate batches indicating good batch-to-batch reproducibility in properties.

Figure 11 shows fractographs of LMJ A356-T6 fatigue samples tested at the maximum stresses of 70 and 75 MPa. The fatigue fracture surfaces have commonalties with the tensile fracture surfaces of vertical LMJ A356-T6 samples (Fig. 9e-f); track and droplet boundaries are seen on the fracture surfaces implying that fatigue cracks propagated along layer boundaries. In case of the 70 MPa sample (Fig. 11a), a single primary crack propagated along the same layer boundary until fracture was complete. Two primary fatigue cracks propagated along two parallel layer boundaries in the

75 MPa sample which resulted in the stepped fracture surface visible in Fig. 11d. A closer examination of the fracture surface in Fig. 11a shows that the track and droplet boundaries are smeared in some regions and sharper in the other regions. The regions with smeared boundaries are those of fatigue crack propagation as confirmed by the presence of fatigue striations (Fig. 11b insert). Rubbing of the opposing fracture surfaces under fully reversed fatigue cycles could explain the smeared and poorly resolved boundaries. The regions with sharply resolved track and droplet boundaries (Fig. 11c) are identical to the tensile fracture surface (Fig. 9e-f) suggesting that final rupture occurred in this region. A visual inspection of all fatigue samples indicated a mode of fatigue crack propagation similar to the samples observed under SEM (Fig. 11) i.e., fatigue crack propagation along the layer boundaries.

Although it is evident that fatigue cracks propagated along layer boundaries, it is difficult to identify crack initiation sites in the fractographs. The cross-sectional microstructure of the 70 MPa fatigue sample in Fig. 12 shows a secondary fatigue crack that initiated from a lack-of-fusion defect at a layer boundary. The fatigue crack in Fig. 12 indicates that lack-of-fusion defects are potential sites for fatigue crack initiation and, thus, the primary fatigue cracks could have also initiated at such defects. The secondary fatigue crack continued to propagate along the layer boundary which is consistent with the fractography in Fig. 11. The crack in Fig. 12 appears to have locally arrested at a Si particle located at the layer boundary.

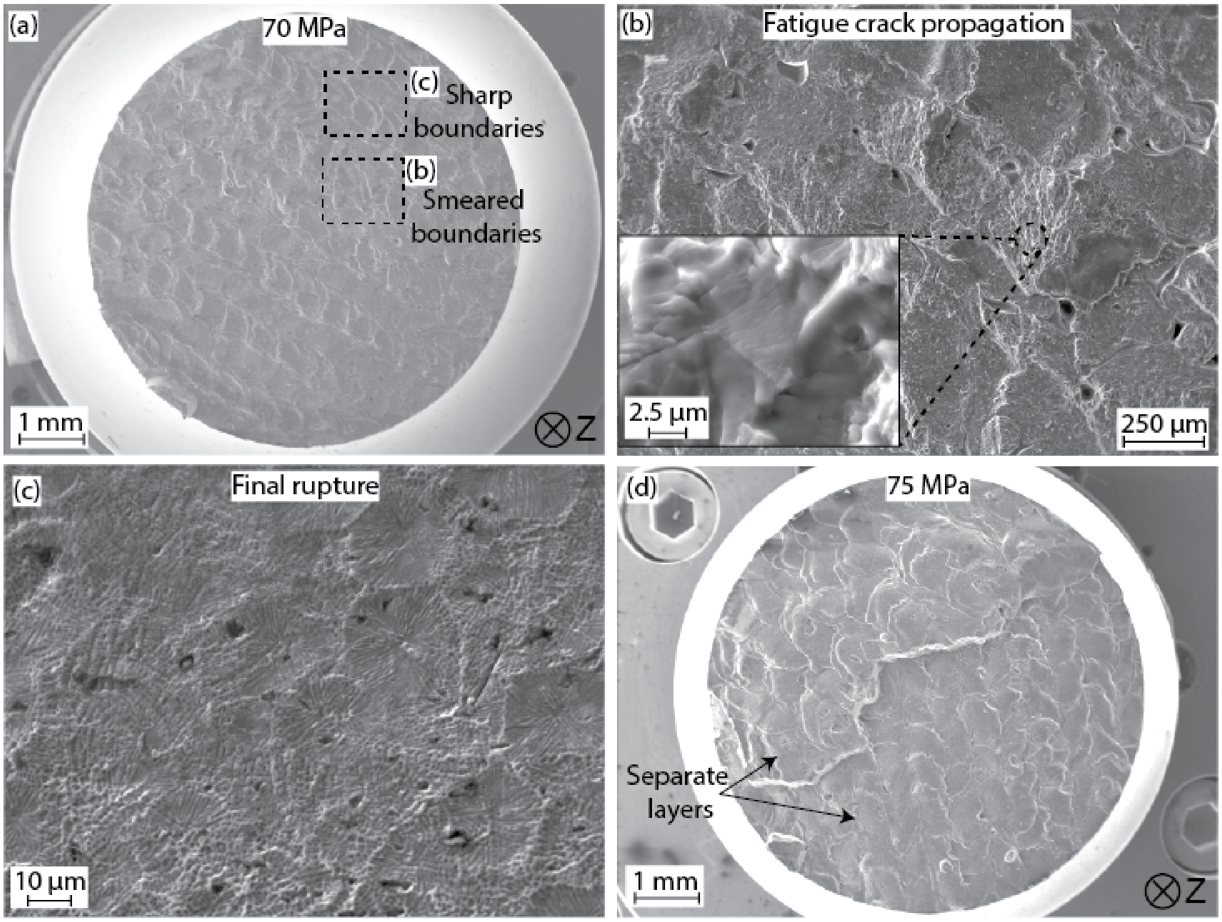

Figure 11 SEM fractographs of vertical LMJ A356-T6 fatigue samples tested at (a-c) 70 MPa and (d) 75 MPa. The images in (b) and (c) are magnified views of the corresponding regions marked in (a). The insert in (b) shows a high magnification view of fatigue striations.

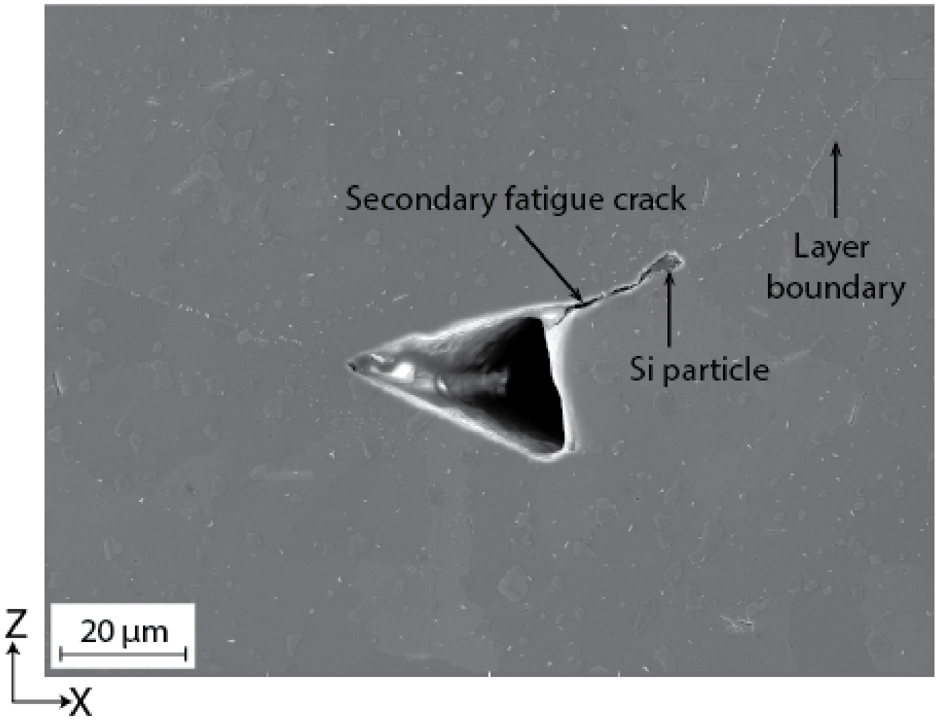

Figure 12 Cross-sectional SEM image of a vertical LMJ A356-T6 fatigue sample tested at 70 MPa showing a secondary fatigue crack initiated at a lack-of-fusion defect on a layer boundary and propagating along the same boundary. The crack seems to have locally arrested at a Si particle.

4. Discussion

4.1. Solidification microstructure

4.1.1. Cooling rate, dendrite arm spacing, and grain structure

Sub-mm size droplets in LMJ are expected to solidify relatively quickly due to their small volume compared to bulk castings with larger volumes and slower solidification. Primary aluminum dendrites and interdendritic Al-Si eutectic form during solidification of an A356 alloy. Eutectic Si forms either as plate-like or fibrous particles in traditional castings [34]. The morphology of Si particles immediately upon solidification is unknown in LMJ, but in situ annealing spheroidizes Si particles in the final microstructure. Spacing between Si particles can be used to estimate droplet cooling rates in LMJ, due to the relationship between cooling rate and secondary dendrite arm spacing (SDAS). The periodic spacing of Si particles (Fig. 3a) makes it possible to approximate SDAS with Si inter-particle spacing for the purpose of estimating the cooling rates; however, it should be noted that this is an extrapolation from the original casting conditions for which such relationships were developed. Jeon and Bae [35] provide a relationship $\lambda_{SDAS} = 40.165 \times C^{-0.415}$, with C being the cooling rate during solidification and λ_{SDAS} being the SDAS. Equating the SDAS with the inter-particle Si spacing yields a mean of $1.6\ \mu m$ with a standard deviation of $0.50\ \mu m$. This corresponds to a cooling rate between $1.2 \times 10^{3} - 6.0 \times 10^{4}$ K/s which agrees with the droplet cooling rates predicted in the study by Gilani et al. [4]. The estimated cooling rate in LMJ is faster than casting (10^{0}-10^{2} K/s) but slower than LPBF AM (10^{5}-10^{6} K/s) [36]. It is noted that the estimated cooling rate is specific to the processing conditions used in the current work. The cooling rate is expected to change with processing conditions such as droplet size, liquid metal superheat, build temperature, and others. Figure S4 compares the microstructures of a cast 356 alloy (higher impurity variant of A356) [20] and LMJ A356 in T6 condition. Solutionizing during T6 treatment leads to similar Si particle sizes in cast and LMJ microstructures; however, faster cooling rates in LMJ refine the interdendritic spacing which in turn produces a uniform distribution of Si particles.

Although LMJ microstructure is largely uniform, some heterogeneity in the microstructure within a single droplet can be observed. In Figure 2d, smaller equiaxed grains can be seen near the boundaries of each droplet with the equiaxed grains increasing in size away from the boundaries. This feature could be compared with the chill zone in a casting, where cooling rates are higher during initial solidification due to conduction into the mold walls. This scenario creates a repeated heterogeneous grain structure at the droplet-scale in the as-fabricated parts.

4.1.2. Formation of defects

Lack-of-fusion defects and shrinkage porosity are the two main types of defects observed in LMJ A356. The mechanisms that lead to lack-of-fusion defects in LMJ have been previously studied [6, 37, 38]. Gas entrapment is one of the reasons for lack-of-fusion defects. Ambient air film (including Ar gas in the current case) on the surface of a substrate can get entrapped upon droplet deposition. This air film pushes the liquid metal and eventually reshapes itself in the form of a cavity. Lack-of-fusion defects due to gas entrapment have been reported for Al droplets deposited on a brass substrate in inert Ar atmosphere with low oxygen and water vapor [6]. The lack-of-fusion defect shown in Fig. 4b is likely due to gas entrapment. These defects have a relatively straight bottom surface facing the layer boundary and a spherical cap formed by the air pushing the liquid metal upwards.

Incomplete fusion between overlapping droplets also leads to defects. Various reasons have been proposed in literature that can cause lack-of-fusion defects. One of the causes is related to ripples that develop in a droplet upon impacting the substrate. The ripples can freeze in place as the droplet solidifies. Incomplete filling of the troughs in the rippled surface produces lack-of-fusion defects [7, 39, 40]. However, it is uncertain if this factor leads to lack-of-fusion in the current case. A droplet solidification contact angle greater than 90° is another factor that leads to lack-of-fusion defects. In this case, lack-of-fusion defects form at the base of overlapping droplets with a triangular morphology [7, 39]. The solidification contact angle of the droplets with the lack-of-fusion defect in Fig. 4a is greater than 90°, setting the condition for defect formation. The spreading of a liquid droplet after impact on a substrate goes through various phases with continuously varying contact angle [7]. The droplet-substrate contact line can freeze during different spreading phases depending on the local thermal conditions which determines the final solidification contact angle. It is possible that local variability in thermal conditions increased droplet solidification contact angle and produced lack-of-fusion defects in Fig. 4a. Other lack-of-fusion defects have an inverted triangular morphology (Fig. 4c). These defects occur when the cusp region between two overlapping droplets in one layer is incompletely filled by the droplet deposited in the next layer. Multiple factors can contribute to such defects. For instance, higher droplet solidification contact angle or larger inter-droplet spacing will deepen the cusp, thereby increasing the chances of incomplete filling. The scan rotation angle is likely to influence filling of the cusp region and in turn defect formation.

The inner regions of droplets contain shrinkage porosity (Fig. 4d). Shrinkage porosity forms when thermal contraction upon solidification is combined with restricted liquid feeding in the last stages of solidification [41]. Computationally, it has been shown that solidification in a droplet begins from the interfaces with the substrate and previously solidified droplet and moves inward within the droplet [3]. It is expected that thermal gradients would decrease as solidification continues from the outside to the inside of the droplet. As the gradient drops, the mushy zone increases in size, increasing the tortuosity for feeding liquid into the interdendritic region and increasing the propensity for pore formation.

This work presents a preliminary understanding of defect formation in LMJ. The three different types of defects identified in the current study include those due to gas entrapment, lack-of-fusion, and shrinkage porosities. A better understanding is required of the relationships between processing parameters and defect formation for each defect type in larger 3-dimensional LMJ structures in order to design approaches for defect management.

4.2. Microstructure-property relationships

4.2.1. Tensile properties

LMJ A356 tensile properties are benchmarked against cast A356 and LPBF A357 alloys (Table 3). LMJ A356 yield strength is approximately half of LPBF A357 yield strength in as-fabricated state [33], a part of which could be due to differences in their Mg content (0.4 wt% vs. 0.6 wt%, respectively). Other factors for lower LMJ A356-AF yield strength can be related to (i) slower cooling rates and (ii) higher build temperature (475 °C) compared to LPBF A357 (35 °C build temperature in [33]). As shown in supplementary Fig. S4, faster cooling rate and lower build temperature in LPBF leads to a closed cellular microstructure with α-Al cells and Al-Si eutectic cellular walls. The cellular microstructure is reported to have a strong Hall-Petch type strengthening effect [42] while such a strengthening mechanism is unavailable in LMJ A356 microstructure with spheroidized Si particles. High dislocation density in LPBF alloys [43, 44] due to faster cooling rates and lower build temperatures provide strengthening; dislocation strengthening is expected to be low in LMJ A356 as slower cooling rates and higher build temperature would prevent buildup of high dislocation density. Faster LPBF cooling rates also increase solute supersaturation and contribute to strength *via* solid solution strengthening [43]. Additional microstructural characterization coupled with modelling of strengthening mechanisms is needed to identify the dominant microstructural feature lowering the as-fabricated yield strength of LMJ A356. The yield strength in LMJ A356 and LPBF A357 increases after the T6 treatment due to precipitation of nanoscale Mg-Si strengthening phases (Table 3). The T6 treatment normalizes the microstructural differences between LMJ A356 and LPBF A357 which are similar post-treatment (supplementary Fig. S4). LMJ A356, LPBF A357, and cast A356 exhibit similar yield strength in T6 condition as the yield strength is mainly determined by Mg-Si nanoscale precipitates while the initial solidification microstructure becomes less important.

LMJ A356-AF samples are isotropic with similar ductility in vertical and horizontal directions. The lower yield strength in LMJ A356-AF also corresponds with the higher ductility. In contrast, LMJ A356-T6 samples are anisotropic with lower ductility in the vertical direction (Fig. 8, Table 3). The anisotropic ductility in LMJ A356-T6 is related to the orientation of layer boundaries with respect to the loading axis. Layer boundaries are aligned parallel to the loading axis in horizontal samples. As a result, cracks that initiates along these boundaries by shear failure are compelled to grow parallel to the loading axis. Since it is difficult for a crack to grow parallel to the loading direction, fracture eventually occurs by typical ductile failure without localizing in the layer boundaries. Cracks in vertical samples grow uninterrupted by delamination along layer boundaries as the layer boundaries are oriented normal to the loading axis. The easy growth of cracks along layer boundaries leads to lower ductility in the vertical direction. Layer boundaries do not influence fracture of LMJ A356-AF vertical samples (Fig. 9a). As a result, vertical and horizontal LMJ A356-AF samples exhibits similar ductility.

LMJ A356 contains a heterogeneous grain structure which can be advantageous for tensile properties [45]. Future work investigating strain partitioning between finer and coarser grains during tensile deformation with EBSD and back stress measurements can explain the effect of heterogeneous grain structure on LMJ A356 tensile properties.

4.2.2. Fatigue properties

LMJ A356-T6 shows a lower fatigue resistance than LPBF A357-T6 and cast A356-T6(a) and (b) alloys (Fig. 10) despite similar tensile properties (Table 3). Fatigue crack initiation and fatigue crack propagation constitute total fatigue lifetime. The cross-sectional microstructure in Fig. 12 suggests that fatigue cracks initiated from lack-of-fusion defects at layer boundaries. Rao et al. [30] reported that defects which initiated fatigue cracks in LPBF A357-T6 (shown in Fig. 10) were less than 100 µm in length. The defects in LMJ A356 are larger than 100 µm (Fig. 5) which is consistent with the lower fatigue strength compared to LPBF A357 containing smaller defects. In the case of cast A356-T6 (b), fatigue cracks initiated at pores with 100-300 µm equivalent diameter which are similar to the defect size in LMJ A356 (Fig. 5). These comparisons indicate that factors other than defect size also influence LMJ A356-T6 fatigue resistance. Unlike the cast microstructure, continuous, oxide-covered layer boundaries spanning the entire cross-section of fatigue samples provide an easy path for fatigue crack propagation in LMJ A356-T6 (Fig. 11). Thus, lack-of-fusion defects which initiate fatigue cracks and layer boundaries which accelerate fatigue crack propagation lower the fatigue resistance of LMJ A356-T6. We hypothesize that fatigue crack is not expected to propagate along layer boundaries in a horizontal sample as the oxide-covered layer boundaries will be parallel to the loading axis. However, a defect should still be the initiator of a fatigue crack in the horizontal sample. Future work comparing fatigue lives and crack growth rates in vertical and horizontal directions can deconvolute individual contributions of defects and oxide film in limiting the fatigue resistance of LMJ A356 alloy.

4.3. Role of oxide film and implications for future research

Oxide film weakens the layer boundaries which then delaminate under monotonic tensile and fatigue loading. The oxide film prevents metallurgical bonding between layers and introduces a metal-oxide interface with certain interfacial strength. Layer boundaries do not delaminate in vertical LMJ A356-AF tensile samples. The lower UTS (165 MPa) of vertical LMJ A356-AF samples ensures that stress at layer boundaries does not exceed the metal-oxide interfacial tensile strength. Much higher stress is applied to vertical LMJ A356-T6 samples due to their higher UTS. As a result, layer boundaries delaminate in vertical LMJ A356-T6 samples. Shear failure at layer boundaries in horizontal LMJ A356-AF and LMJ A356-T6 tensile samples alludes to low shear strength of the metal-oxide interface. Layer delamination is not expected in vertical LMJ A356-T6 fatigue samples because of lower applied stresses. The maximum cyclic stresses in fatigue tests (60 – 150 MPa) are lower than the maximum stress (i.e., UTS of 165 MPa) experienced by vertical LMJ A356-AF tensile samples where no delamination occurs. Yet, fatigue cracks propagate by delamination of layer boundaries possibly due to local stress concentration at fatigue crack tips.

The challenge of metal-oxide interfacial delamination can be exasperated by PFZs at the oxide film (Fig. 7). Strain localization in soft PFZs makes them a preferred fracture site in Al alloy microstructures [46-48]. By a similar mechanism, strain localization in PFZs can increase local stress concentration at the metal-oxide interface and promote delamination. One of the mechanisms for PFZ formation in Al alloys is attributed to growth of grain-boundary precipitates. Grain-boundary precipitates grow by consuming solutes from the nearby matrix and the depleted matrix can no longer form the strengthening precipitates. The PFZs of interest in this study are related to the oxide film instead of grain-boundaries. The oxide film is enriched in Mg and Si and its growth can deplete these solutes in the nearby Al matrix resulting in PFZs. Indeed, APT results have shown that the matrix near the oxide is depleted in Mg and Si (Table 2). Mg and Si enrichment in the oxide layer could occur in the inception stage itself when the liquid droplet surface is oxidizing. Alternatively, Mg and Si could diffuse into the oxide during solutionizing stage of the T6 treatment.

The research in LMJ manufactured alloys is in a nascent stage with very little known about the microstructure-property relationships. The relatively lower fatigue resistance of LMJ alloy should not be construed as an inherent weakness of LMJ additive manufacturing. This work expects to motivate research aimed at mitigating the negative influence of oxide film on mechanical performance of LMJ alloys while benefiting from the processing advantages offered by LMJ. The liquid metal droplets are shielded with Ar gas during LMJ printing, but the results of this study show that it is insufficient to prevent oxidation. The oxide film makes the layer boundaries sites for fracture, however, the impact on tensile properties is limited considering that the strength and ductility of LMJ A356-T6 are similar to cast A356-T6 (Table 3). The oxide film has a more severe impact on limiting the fatigue resistance of LMJ A356 (Fig. 10). Future research on LMJ additive manufacturing should focus on minimizing oxidation. An obvious solution is to conduct the process in a fully inert chamber or under high vacuum with potential trade-offs related to cost and process complexity. On the other hand, (1) optimizing process parameters, (2) optimizing heat-treatments, and (3) alloy design may help alleviate the oxidation problem. Metal-oxide interfacial delamination is observed only at layer boundaries but not at transversely oriented track boundaries and inter-droplet boundaries which are also expected to be oxidized. This observation indicates that the oxide continues to grow after droplet deposition with the growth sustained possibly by the high build temperature. The time interval between deposition of two overlapping droplets in the same track and deposition of two overlapping tracks in the same layer is less compared to that between deposition of two overlapping layers. The larger time interval between deposition of two layers can provide more time for the oxide film to thicken at the layer boundary and reduce the material resistance to failure. Thus, optimizing the thermal energy of the system by adjusting the build temperature and/or the temperature of the liquid metal to minimize oxide growth without compromising droplet fusion may improve the mechanical properties. The oxide film negatively impacts ductility more so in the T6 condition than the as-fabricated condition (Fig. 9a vs. Fig. 9e). This result emphasizes the need to design LMJ-suited heat treatments. New alloys can be designed for LMJ with better resistance to oxidation. Alloying elements that form nanoscale strengthening precipitates but do not incorporate into the oxide may suppress PFZ formation and offer improvement in mechanical properties.

5. Conclusions

An A356 (Al-7Si-0.4Mg, wt%) alloy is additively manufactured with droplet-on-demand liquid metal jetting (DOD-LMJ). The microstructure, tensile, and fatigue properties of LMJ A356 are characterized in the as-fabricated and T6-aged conditions. The role of droplet oxidation on the tensile and fatigue properties is discussed. The key conclusions drawn are as follows:

1. The as-fabricated microstructure consists of uniformly dispersed Si particles of ~ 0.5 µm diameter and fine equiaxed grains with a 10 µm average diameter. The high build plate temperature of 475 °C spheroidizes Si particles formed upon droplet solidification.
2. Atom probe tomography revealed that the layer boundaries are covered with a few nanometers thick (Al-Mg-Si)-O oxide film despite Ar gas shielding.
3. The yield strength and ductility are isotropic in the as-fabricated condition at ~ 110 MPa, and 18 – 21%, respectively. After T6 aging, the yield strength is isotropic (~ 250 MPa), but the ductility is lower in the build direction (6.1 ± 1.4%) compared to that in the transverse direction (9.4 ± 1.0%). The lower ductility in the build direction is due to delamination of the metal-oxide interface at the layer boundaries.
4. LMJ A356 exhibits 60 MPa of fatigue strength in T6 condition. The fatigue resistance is limited by (i) fatigue crack initiation at lack-of-fusion defects and (ii) fatigue crack propagation along oxide-covered layer boundaries.

Acknowledgements

The research was sponsored by the U.S. Department of Energy, Office of Energy Efficiency and Renewable Energy (EERE) through the Powertrain Materials Core Program of Vehicle Technologies Office and Manufacturing Demonstration Facility which is a EERE user facility supported by Advanced Materials and Manufacturing Technology Office and operated by Oak Ridge National Laboratory. APT research was supported by the Center for Nanophase Materials Sciences, which is a US Department of Energy, Office of Science User Facility at Oak Ridge National Laboratory. The authors would like to thank James Burns for assistance in performing APT sample preparation and running the APT experiments, Kelsey Epps for tensile testing, Shane Hawkins for fatigue testing, Dana McClurg for heat treatments, Brian Long for metallographic sample preparation, and Julio Rojas for x-ray tomography. The authors would also like to thank Jovid Rakhmonov and Holden Hyer for reviewing the manuscript.

References

[1] T.Y. Ansell, Current Status of Liquid Metal Printing, J. Manuf. Mater. Process. 5(2) (2021) 31.
[2] W.J. Sames, F.A. List, S. Pannala, R.R. Dehoff, S.S. Babu, The metallurgy and processing science of metal additive manufacturing, Int. Mater. Rev. 61(5) (2016) 315-360.
[3] H. Li, P. Wang, L. Qi, H. Zuo, S. Zhong, X. Hou, 3D numerical simulation of successive deposition of uniform molten Al droplets on a moving substrate and experimental validation, Comput. Mater. Sci. 65 (2012) 291-301.
[4] N. Gilani, N.T. Aboulkhair, M. Simonelli, M. East, I. Ashcroft, R.J.M. Hague, Insights into drop-on-demand metal additive manufacturing through an integrated experimental and computational study, Addit. Manuf. 48 (2021) 102402.
[5] Y. Dou, J. Luo, L. Qi, H. Lian, J. Huang, Drop-on-demand printing of recyclable circuits by partially embedding molten metal droplets in plastic substrates, J. Mater. Process. Technol. 297 (2021) 117268.
[6] H. Yi, L.-h. Qi, J. Luo, Y. Jiang, W. Deng, Pinhole formation from liquid metal microdroplets impact on solid surfaces, Appl. Phys. Lett. 108(4) (2016).
[7] N. Gilani, N.T. Aboulkhair, M. Simonelli, M. East, I.A. Ashcroft, R.J.M. Hague, From impact to solidification in drop-on-demand metal additive manufacturing using MetalJet, Addit. Manuf. 55 (2022) 102827.
[8] S. Vader, Z. Vader, I.H. Karampelas, E.P. Furlani, Magnetohydrodynamic liquid metal jet printing, TechConnect Conference, 2015, pp. 2-4.
[9] What Xerox's aluminium liquid metal AM offers for supply chain resiliency, 2022. https://www.metal-am.com/articles/what-xeroxs-aluminium-liquid-metal-am-3d-printing-offers-for-supply-chain-resiliency/.
[10] M. Orme , R.F. Smith, Enhanced Aluminum Properties by Means of Precise Droplet Deposition, Journal of Manufacturing Science and Engineering 122(3) (1999) 484-493.
[11] M. Orme, Q. Liu, R. Smith, Molten aluminum micro-droplet formation and deposition for advanced manufacturing applications, Aluminum Transactions 3(1) (2000) 95-103.
[12] V. Sukhotskiy, I.H. Karampelas, G. Garg, A. Verma, M. Tong, S. Vader, Z. Vader, E.P. Furlani, Magnetohydrodynamic drop-on-demand liquid metal 3D printing, (2017).
[13] B. Gerdes, R. Zengerle, P. Koltay, L. Riegger, Direct printing of miniscule aluminum alloy droplets and 3D structures by StarJet technology, Journal of Micromechanics and Microengineering 28(7) (2018) 074003.
[14] W. Cao, Y. Miyamoto, Freeform fabrication of aluminum parts by direct deposition of molten aluminum, J. Mater. Process. Technol. 173(2) (2006) 209-212.
[15] T. Metz, G. Birkle, R. Zengerle, P. Koltay, StarJet: Pneumatic Dispensing of Nano- to Picoliter Droplets of Liquid Metal, 2009 IEEE 22nd International Conference on Micro Electro Mechanical Systems, 2009, pp. 43-46.
[16] https://additec3d.com/liquid-metal-jetting-elemx/.
[17] N.N. Watkins, K.D. Traxel, A.E. Wilson-Heid, T.C. Reeve, C.M. Silva, J.R. Jeffries, A.J. Pascall, Process-structure-property relationships for droplet-on-demand liquid-metal-jetted parts, Addit. Manuf. 73 (2023) 103709.

[18] K.D. Traxel, A.E. Wilson-Heid, N. N. Watkins, C. M. Silva, J.R. Jeffries, A. J. Pascall, Microstructure and tensile properties of droplet-on-demand additively manufactured AlSi7Mg, Addit. Manuf. 87 (2024) 104215.
[19] V. Sukhotskiy, K. Tawil, E. Einarsson, Printability regimes of pure metals using contactless magnetohydrodynamic drop-on-demand actuation, Phys. Fluids 33(5) (2021).
[20] S. Roy, L.F. Allard, A. Rodriguez, T.R. Watkins, A. Shyam, Comparative evaluation of cast aluminum alloys for automotive cylinder heads: Part I—microstructure evolution, Metall. Mater. Trans. A 48(5) (2017) 2529-2542.
[21] K. Thompson, D. Lawrence, D.J. Larson, J.D. Olson, T.F. Kelly, B. Gorman, In situ site-specific specimen preparation for atom probe tomography, Ultramicroscopy 107(2) (2007) 131-139.
[22] S. Bahl, T. Wu, R.A. Michi, K. An, D. Yu, L.F. Allard, J.U. Rakhmonov, J.D. Poplawsky, C.M. Fancher, D.C. Dunand, A. Plotkowski, A. Shyam, An additively manufactured near-eutectic Al-Ce-Ni-Mn-Zr alloy with high creep resistance, Acta Mater. 268 (2024) 119787.
[23] METALLOGRAPHY GUIDE FOR XEROX® 4008 ALUMINUM WIRE. https://www.xerox.com/downloads/usa/en/3d-printing/ElemX-Metallography-Guide.pdf.
[24] R. Vissers, M.A. van Huis, J. Jansen, H.W. Zandbergen, C.D. Marioara, S.J. Andersen, The crystal structure of the β′ phase in Al–Mg–Si alloys, Acta Mater. 55(11) (2007) 3815-3823.
[25] G. Sha, H. Möller, W.E. Stumpf, J.H. Xia, G. Govender, S.P. Ringer, Solute nanostructures and their strengthening effects in Al–7Si–0.6Mg alloy F357, Acta Mater. 60(2) (2012) 692-701.
[26] C.D. Marioara, S.J. Andersen, J. Jansen, H.W. Zandbergen, Atomic model for GP-zones in a 6082 Al–Mg–Si system, Acta Mater. 49(2) (2001) 321-328.
[27] K. Matsuda, T. Naoi, K. Fujii, Y. Uetani, T. Sato, A. Kamio, S. Ikeno, Crystal structure of the β′′ phase in an Al–l.0mass%Mg2Si–0.4mass%Si alloy, Mater. Sci. Eng., A 262(1) (1999) 232-237.
[28] M. Jobba, R.K. Mishra, M. Niewczas, Flow stress and work-hardening behaviour of Al–Mg binary alloys, Int. J. Plast. 65 (2015) 43-60.
[29] M. Lebyodkin, L. Dunin-Barkowskii, Y. Bréchet, Y. Estrin, L.P. Kubin, Spatio-temporal dynamics of the Portevin–Le Chatelier effect: experiment and modelling, Acta Mater. 48(10) (2000) 2529-2541.
[30] J.H. Rao, Y. Zhang, A. Huang, X. Wu, K. Zhang, Improving fatigue performances of selective laser melted Al-7Si-0.6Mg alloy via defects control, Int. J. Fatigue 129 (2019) 105215.
[31] A. Shyam, J.A. Haynes, G. Black, J. Talamantes, High Performance Cast Aluminum Alloys for Next Generation Passenger Vehicle Engines, Oak Ridge National Lab.(ORNL), Oak Ridge, TN (United States), 2018.
[32] J.Z. Yi, Y.X. Gao, P.D. Lee, T.C. Lindley, Microstructure-based fatigue life prediction for cast A356-T6 aluminum-silicon alloys, Metallurgical and Materials Transactions B 37(2) (2006) 301-311.
[33] K.V. Yang, P. Rometsch, C.H.J. Davies, A. Huang, X. Wu, Effect of heat treatment on the microstructure and anisotropy in mechanical properties of A357 alloy produced by selective laser melting, Mater. Des. 154 (2018) 275-290.
[34] S.D. McDonald, K. Nogita, A.K. Dahle, Eutectic nucleation in Al–Si alloys, Acta Mater. 52(14) (2004) 4273-4280.
[35] J.H. Jeon, D.H. Bae, Effect of cooling rate on the thermal and electrical conductivities of an A356 sand cast alloy, J. Alloys Compd. 808 (2019) 151756.

[36] T. DebRoy, H.L. Wei, J.S. Zuback, T. Mukherjee, J.W. Elmer, J.O. Milewski, A.M. Beese, A. Wilson-Heid, A. De, W. Zhang, Additive manufacturing of metallic components – Process, structure and properties, Prog. Mater. Sci. 92 (2018) 112-224.
[37] M. Meda, V. Sukhotskiy, D. Cormier, Pinhole Formation in Printed Electronic Traces Fabricated via Molten Metal Droplet Jetting, Electronics 10(13) (2021) 1568.
[38] H. Yi, Z. Wang, H. Cao, M. Liu, J. Li, Metal Droplet Deposition: From Foundation to Engineering Manufacturing, Adv. Eng. Mater. 25(3) (2023) 2201003.
[39] H. Yi, L. Qi, J. Luo, D. Zhang, H. Li, X. Hou, Effect of the surface morphology of solidified droplet on remelting between neighboring aluminum droplets, International Journal of Machine Tools and Manufacture 130-131 (2018) 1-11.
[40] Y. Dou, J. Luo, L. Qi, L. Su, H. Lian, J. Huang, Quantitatively characterizing the evolution of hole defects between overlapped aluminum droplets by a two-dimensional solidification model, Addit. Manuf. 60 (2022) 103202.
[41] J.A. Dantzig, M. Rappaz, Solidification: -Revised & Expanded, EPFL press2016.
[42] Y.M. Wang, T. Voisin, J.T. McKeown, J. Ye, N.P. Calta, Z. Li, Z. Zeng, Y. Zhang, W. Chen, T.T. Roehling, R.T. Ott, M.K. Santala, Philip J. Depond, M.J. Matthews, A.V. Hamza, T. Zhu, Additively manufactured hierarchical stainless steels with high strength and ductility, Nat. Mater. 17(1) (2018) 63-71.
[43] R. Jain, M. Yadava, N. Nayan, N.P. Gurao, Combinatorial synchrotron diffraction-constitutive modelling-crystal plasticity simulation framework for direct metal laser sintered AlSi10Mg alloy, Materialia 22 (2022) 101395.
[44] S. Bahl, S. Mishra, K.U. Yazar, I.R. Kola, K. Chatterjee, S. Suwas, Non-equilibrium microstructure, crystallographic texture and morphological texture synergistically result in unusual mechanical properties of 3D printed 316L stainless steel, Addit. Manuf. 28 (2019) 65-77.
[45] Y. Zhu, K. Ameyama, P.M. Anderson, I.J. Beyerlein, H. Gao, H.S. Kim, E. Lavernia, S. Mathaudhu, H. Mughrabi, R.O. Ritchie, N. Tsuji, X. Zhang, X. Wu, Heterostructured materials: superior properties from hetero-zone interaction, Mater. Res. Lett. 9(1) (2021) 1-31.
[46] A.K. Vasudévan, R.D. Doherty, Grain boundary ductile fracture in precipitation hardened aluminum alloys, Acta Metall. 35(6) (1987) 1193-1219.
[47] J.U. Rakhmonov, S. Bahl, A. Shyam, D.C. Dunand, Cavitation-resistant intergranular precipitates enhance creep performance of θ′-strengthened Al-Cu based alloys, Acta Mater. (2022) 117788.
[48] W. Sun, Y. Zhu, R. Marceau, L. Wang, Q. Zhang, X. Gao, C. Hutchinson, Precipitation strengthening of aluminum alloys by room-temperature cyclic plasticity, Science 363(6430) (2019) 972.